Front. Environ. Sci. Eng. 2022, 16(11): 144
https://doi.org/10.1007/s11783-022-1579-7

RESEARCH ARTICLE

Adsorption of herring sperm DNA onto pine sawdust biochar: Thermodynamics and site energy distribution

Mingyi Yang[1], Lin Shi[2], Di Zhang (✉)[2,3], Zhaohui He[1], Aiping Liang[4], Xiao Sun[1]

1 Faculty of Environmental Science and Engineering, Kunming University of Science and Technology, Kunming 650500, China
2 School of Resources and Environment, Linyi University, Linyi 276005, China
3 Yunnan Provincial Key Laboratory of Soil Carbon Sequestration and Pollution Control, Kunming 650500, China
4 School of Environmental and Material Engineering, Yantai University, Yantai 264005, China

HIGHLIGHTS

- Adsorption of environmental deoxyribonucleic acid on biochar was studied.
- π–π interaction and electrostatic repulsion worked in the adsorption.
- Thermodynamics indicated the adsorption was spontaneous and endothermic.

GRAPHIC ABSTRACT

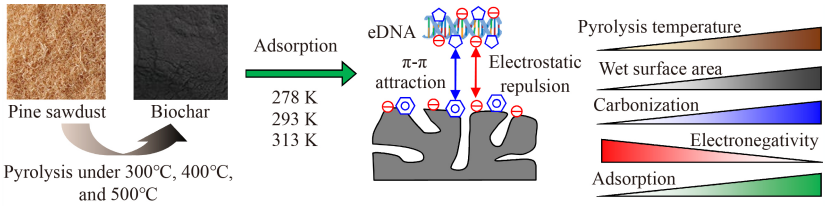

ARTICLE INFO

Article history:
Received 12 January 2022
Revised 11 March 2022
Accepted 12 April 2022
Available online 5 June 2022

Keywords:
Environmental deoxyribonucleic acid
Antibiotic resistance genes
Biochar
Adsorption thermodynamics

ABSTRACT

Environmental deoxyribonucleic acid (eDNA), which includes antibiotic resistance genes, is ubiquitous in the environment. The interactions between eDNA and biochar, a promising material widely used in soil amendment and water treatment, greatly affect the environmental behavior of eDNA. Hitherto few experimental evidences are available yet, especially on the information of thermodynamics and energy distribution to explains the interactions between biochar and eDNA. This study investigated the adsorption of herring sperm DNA (hsDNA) on pine sawdust biochar, with a specific emphasis on the adsorption thermodynamics and site energy distribution. The adsorption of hsDNA on biochar was enhanced by an increase in the pyrolysis and adsorption temperatures. The higher surface area, stronger π–π interaction, and weaker electrostatic repulsion between hsDNA and biochars prepared at high pyrolysis temperatures facilitated the adsorption of hsDNA. The thermodynamics indicated that the adsorption of hsDNA on biochar was spontaneous and endothermic. Therefore, higher temperature was beneficial for the adsorption of hsDNA on biochar; this was well explained by the increase in E^* and $F(E^*)$ with the adsorption temperature. These results are useful for evaluating the migration and transformation of eDNA in the presence of biochar.

1 Introduction

Environmental deoxyribonucleic acid (eDNA) refers to the DNA mainly secreted from living cells or released from dead organisms (Zhang et al., 2019). Upon entering a terrestrial or aquatic ecosystem, eDNA plays various positive or negative roles. For example, eDNA is an important carbon/phosphorus source for microbes to maintain metabolism and reproduction (Levy-Booth et al., 2007); however, antibiotic resistance genes, an essential component of eDNA, cause the unquenchable spread of antimicrobial resistance (Pruden et al., 2006) due to their diffusion in microbial communities via intergenerational transmission and horizontal transfer (Zhou et al., 2021). Hence, the environmental and ecological effects of eDNA have attracted extensive attention, because of the ubiquity and stability of such DNA (Pietramellara et al., 2007).

Previous studies have mainly focused on eDNA adsorption on natural minerals, which then control the environmental and ecological effects of eDNA. On the one hand, eDNA adsorption on minerals was found to be dependent on the molecular structure of eDNA. For example, Wu et al. (2018) found that the adsorption site of eDNA was mainly the phosphate group on the outer side of the double helix structure. Supercoiled eDNA

✉ Corresponding author
E-mail: zhangdi2002113@sina.com

adsorbed less than linear eDNA because the phosphate groups were trapped inside the eDNA molecules and were hence not accessible (Poly et al., 2000). On the other hand, the types and properties of natural minerals were also found to be key factors that affected eDNA adsorption. For example, compared with montmorillonite, kaolin has more hydroxyl groups on the outer alumina octahedron, and hence higher adsorption capacity for the phosphoric acid skeleton of eDNA (Gardner and Gunsch, 2017). For the same reason, eDNA adsorbs more on metal oxides than clays (owing to the more active hydroxyl groups on metal oxide surfaces) (Cai et al., 2008). Generally, cation bridging (Sheng et al., 2019), ligand exchange (Schmidt and Martínez, 2017), hydrogen bonding (Yu et al., 2013), and electrostatic interaction (Min et al., 2014) are considered the major mechanisms for eDNA adsorption on natural minerals.

Biochar, an environmentally friendly material, has been extensively utilized for soil carbon sequestration (Dong et al., 2019), soil amelioration, and pollution control (Liu et al., 2018b). Biochar is endowed with high adsorption capacity for various pollutants owing to its large surface area, abundant functional groups, and porous structure (Teixidó et al., 2011; Yin et al., 2016). The extensive application of biochar into soil will inevitably affect the interactions between eDNA and minerals, resulting in unforeseeable environmental behaviors of eDNA. To our knowledge, very few studies have focused on eDNA adsorption on biochar. Wang et al. (2014a) proposed that the micropore surface area is the main factor that influences eDNA adsorption on biochar, despite the mechanisms not being ascertained yet. Nevertheless, it is notable that the molecular volume of eDNA is far higher than that of traditional contaminants; therefore, the micropores of biochar may be inaccessible to eDNA (Poly et al., 2000). Lian et al. (2020) also suggested that eDNA adsorption on biochar is mainly dependent on surface adsorption, rather than micropore filling. Apparently, the understanding on eDNA adsorption on biochar is fragmented, unclear, and even contradictory.

The thermodynamics of the adsorption process is critical for understanding adsorption mechanisms. Cai et al. (2008) found that DNA adsorption on hydroxyl aluminum−montmorillonite complexes was exothermic, owing to ligand exchange and hydrogen bonding. In contrast, DNA adsorption was endothermic on pure montmorillonite, owing to the dehydration process. These research deficiencies and contradictions regarding eDNA adsorption on biochar hinder the understanding on eDNA environmental behavior upon the extensive application of biochar.

In this study, DNA from herring sperm (hsDNA) was adopted, because it has been wildly used as a model DNA with stable structure to investigate the interactions with other extracted materials (Zhong et al., 2003), metal materials (Liu et al., 2018a) and biochar (Wang et al., 2014a). Pine sawdust, a typical forestry waste, was used as low-cost and easily available protoplasm to prepare biochar. The present study was aimed at (1) investigating the possible major mechanisms of eDNA adsorption on biochar and (2) revealing the adsorption thermodynamic characteristics. The results will provide useful information for understanding the environmental behavior of eDNA.

2 Materials and methods

2.1 Chemicals

hsDNA (< 50 bp) was purchased from Sigma−Aldrich, USA (single-stranded for hybridization, CAS No. 100403-24-5). As the genetic material of herring, hsDNA is the double helix structure with a diameter of 2 nm and length of 17 nm. The outer deoxyribose and phosphoric acid are connected alternately to form the basic skeleton, and the bases line up on the inside, exhibiting B-type conformation. Tris base ($C_4H_{11}NO_3$, tris(hydroxymethyl) aminomethane hydrochloride) was purchased from BioFroxx, Germany. hsDNA powder was dissolved in 0.01 mol/L Tris−HCl buffer solution at pH = 7 to maintain the stability of the DNA morphological structure during the experiments. Abs260/Abs280 absorbance ratios in the range of 1.8−1.9 indicated that the purity of eDNA was up to the standard. Deionized water was obtained from an ultrapure water system (Milli-Q Advantage A10, Merck, Germany).

2.2 Preparation and characterization of biochar

Raw pine sawdust was rinsed with ultrapure water and dried in an oven at 90 °C for 48 h. The milled pine sawdust was passed through a 60 mesh screen (0.25 mm) and charred at preset temperatures (300, 400, and 500 °C) for 4 h under limited oxygen conditions. The obtained biochars were washed with ultrapure water to eliminate the interference of soluble components in hsDNA quantification. The final pine sawdust biochars were labeled PS300, PS400, and PS500.

An element analyzer (MicroCube, Elementar, Germany) was used to determine the elemental compositions of the biochars. The ash content was determined by combusting the biochars under 750 °C for 6 h in a muffle furnace (Jiang et al., 2017), and calculating the difference between the residual mass and initial mass. The specific surface area (SSA) and pore size distribution of the biochars were determined using the traditional Brunauer−Emmett−Teller (BET) and Barrett−Joyner−Halenda methods, respectively (Autosorb-1C, Quantachrome, USA). The surface area of biochar exposed to a liquid is proportional to the amounts of boundary water on the biochar surface. The ^{1}H NMR relaxation rate of boundary water on a solid surface is far

higher than that of free water. The amounts of boundary water may be reflected by the enhancement in the relaxation rate of total water (R_{sp}). Hence, R_{sp} represents the surface area of biochar exposed to water, which could be obtained using an Acorn Area analyzer (XiGo Nanotools, USA) to assist in the surface analysis of the biochars (Shi et al., 2021). The detailed principle, calculation and verification can be found in the Supplementary File (Fig. S1). The variations in the surface potentials of the biochars and hsDNA with pH were detected using a zeta potential analyzer (ZetaPlus, Brookhaven, USA). The surface functional groups of the biochars before and after eDNA adsorption were identified using Fourier-transform infrared (FTIR) spectra (Nicolet iS50, Thermo Fisher Scientific, USA), which were recorded in the wave number range of 400−4000 cm^{-1}.

2.3 Adsorption experiment

All the experiments of hsDNA adsorption on biochars were conducted using 8 mL amber vials equipped with Teflon-lined screw caps at 278 ± 1, 293 ± 1, and 313 ± 1 K in parallel. The hsDNA stock solution (60 mg/L) was diluted with the background solution (0.01 mol/L Tris−HCl buffer) to seven different concentrations (2−30 mg/L). Based on a preliminary experiment, the aqueous:solid ratio was fixed at 400:1 (w:w). All the vials were kept in the dark and shaken in a rotary shaker at the three predefined temperatures for 7 d. After centrifugation at 3000 r/min for 10 min, the hsDNA concentration in the supernatant was measured at 260 nm using a UV–Vis spectrophotometer (UV-2600, Shimadzu, Japan).

The Langmuir model (LM, Eq. (1)) and Freundlich model (FM, Eq. (2)) were employed to fit the adsorption isotherms:

$$Q_e = \frac{Q_m K_1 C_e}{1 + K_1 C_e}, \tag{1}$$

$$Q_e = K_f (C_e)^n, \tag{2}$$

where Q_e (mg/g) is the equilibrium adsorption in the solid phase; C_e (mg/L) is the equilibrium solution concentration; K_l (L/mg) and K_f ($mg^{1-1/n} \cdot L^{1/n}/g$) are the adsorption coefficients in LM and FM, respectively; Q_m (mg/g) is the maximum adsorption capacity in LM; and n is the empirical constant for isotherm nonlinearity. The Chi-squared (χ^2) distribution (Chen et al., 2019) was adopted to analyze the fitting quality with the determined coefficient R^2, as shown in Eq. (3):

$$\chi^2 = \sum \left[\frac{(Q_e - Q_x)^2}{Q_x} \right], \tag{3}$$

where Q_x (mg/g) is the calculated equilibrium capacity according to LM or FM. The fitting results of the adsorption isotherms within the same abscissa and ordinate could be compared using the isotherm parameters. Lower values of χ^2 indicate better fitting results.

In order to invest the roles of electrostatic interaction, the adsorption of hsDNA on PS500 at a series of pH was applied. Specifically, 8 mL hsDNA with the concentration of 30 mg/L at pH range of 2−9 was mixed with 20 mg PS500, and the subsequent operation was the same with the isothermal adsorption experiment. In addition, the isothermal adsorption experiment of hsDNA on PS300 and PS400 at pH = 4 was carried out to study the role of π−π interaction. Both experiments were carried out under 298 K.

2.4 Thermodynamic analysis and site energy distribution

The isotherms of eDNA adsorption on biochars at 278, 293, and 313 K were employed to calculate the thermodynamic parameters. Using the classical Van't Hoff equation, the Gibbs free energy change (ΔG, kJ/mol) was determined with the equilibrium coefficient (K_d, L/g), as follows:

$$\Delta G = -RT \ln K_d, \tag{4}$$

$$K_d = \frac{Q_e}{C_e}, \tag{5}$$

where R (8.314×10^{-3} kJ/(mol·K)) is the universal constant, and T (K) is the Kelvin temperature. Standard ΔG is also related to the standard enthalpy change (ΔH, kJ/mol) and standard entropy change (ΔS, J/(mol·K)) as follows:

$$\Delta G = \Delta H - T\Delta S. \tag{6}$$

Combining Eqs. (4) and (6):

$$\ln K_d = \frac{\Delta S}{R} - \frac{\Delta H}{RT}. \tag{7}$$

The values of ΔH and ΔS can be derived from the plot of $\ln K_d$ against $1/T$ based on a least-squares analysis.

The condensation approximation was used to produce approximate energy distribution functions. The approximate site energy distribution of FM is defined using the following function:

$$F(E^*) = \frac{K_f n (C_s)^n}{RT} \exp\left(-\frac{nE^*}{RT}\right). \tag{8}$$

According to the Polanyi adsorption potential theory, the adsorption site energy (E^*, kJ/mol) refers to the difference in adsorption energy at C_e and C_s (mg/L), which is $-RT\ln(C_e/C_s)$, where C_s is the water solubility of the adsorbate.

3 Results and discussion

3.1 Characteristics of pine sawdust biochar

Selected physiochemical properties of the prepared biochars, including ash content, elemental content, and SSA, are tabulated in Table 1. With an increase in pyrolysis temperature, the ash content of biochar increased,

whereas H and O percentages decreased. The higher C content of PS500 indicated its higher carbonization and more condensed carbon structure (Qian et al., 2016). The values of the (O+N)/C and H/C molar ratios decreased in the order PS300 > PS400 > PS500, suggesting a reduction in polarity and an enhancement in aromaticity of biochar with an increase in pyrolysis temperature (Chen et al., 2008).

The enlargement in the SSA of biochar was induced by the increase in pyrolysis temperature (Table 1), consistent with results in the literature (Leng et al., 2021). The pore distributions of the three biochars are shown in Fig. S2. Micropores (<10 nm) and mesopores (10−50 nm) were in the majority, and 3 nm pores had the highest frequency for all three biochars. In addition, the pore distribution of PS300 and PS400 was almost the same. The pore volume of PS500 was the largest, consistent with the SSA. It is notable that the SSA was quantified using the BET method, which could only reflect the surface area of biochar exposed to a gaseous phase. Hence, the surface exposed to water would be more ideal to explain the adsorption behavior in this study. The solvation relaxation based nuclear magnetic resonance technology has been used to measure the wet specific surface area of silica nanoparticles (Yuan et al., 2017) and carbon nanotubes (Pan et al., 2013). Compared with that of pure water, the R_{sp} of the biochar and water mixture could better reflect the amount of boundary water on the biochar surface, and further effectively reflect the interface area between biochar and water (Zhang et al., 2017). The principle is introduced in detail in the Supplementary File. As shown in Fig. 1(a), the larger wet surface area of PS500 was demonstrated by its higher R_{sp} values at a certain biochar concentration, compared with those of PS400 and PS300. k_r (L/mg), the slope of the relationship between R_{sp} and biochar concentration (Ψ, g/mL), was used to reflect the relative magnitudes of the wet surface area more accurately (Table 1). Specifically, the wet surface area of PS500 was 1.9 and 3 times higher than that of PS400 and PS300, respectively.

The surface potentials of the biochars at a series of pH are shown in Fig. 1(b). hsDNA and the surface of biochar gradually became more negatively charged with an increase in pH. In addition, the enhancement in carbonization at the higher pyrolysis temperature resulted in fewer negative charges on the biochar surface at the same pH. The tendency of the decrease in surface electronegativity with an increase in pyrolysis temperature was consistent with that of the decrease in polarity (Hong et al., 2019), reflected by the polarity index (O+N)/C of the biochars (Table 1).

3.2 Isotherms of hsDNA adsorption on biochar

LM (Fig. S3) and FM (Fig. 2) were used to fit the isotherms of hsDNA adsorption on biochars; the fitting parameters are presented in Table 2. Compared with LM, FM better fitted the isotherms of eDNA adsorption on biochars at the three experimental temperatures, as indicated by the higher R^2 values with the lower χ^2 values (Table 2). Therefore, the following discussion is based on the fitting results of FM. hsDNA adsorbed less on biochar

Table 1 Selected physicochemical properties of pine sawdust biochars

Biochar	Ash (%)	Elemental content (%)					Molar ratio		SSA (m^2/g)	k_r (L/mg)
		C	H	O	N	S	(O+N)/C	H/C		
PS300	0.82	62.23	4.95	31.55	0.08	0.08	0.38	0.95	4.09	0.05
PS400	2.00	74.84	3.33	19.92	0.18	0.08	0.20	0.53	4.98	0.08
PS500	3.60	79.90	2.70	14.63	0.24	0.05	0.14	0.41	9.89	0.15

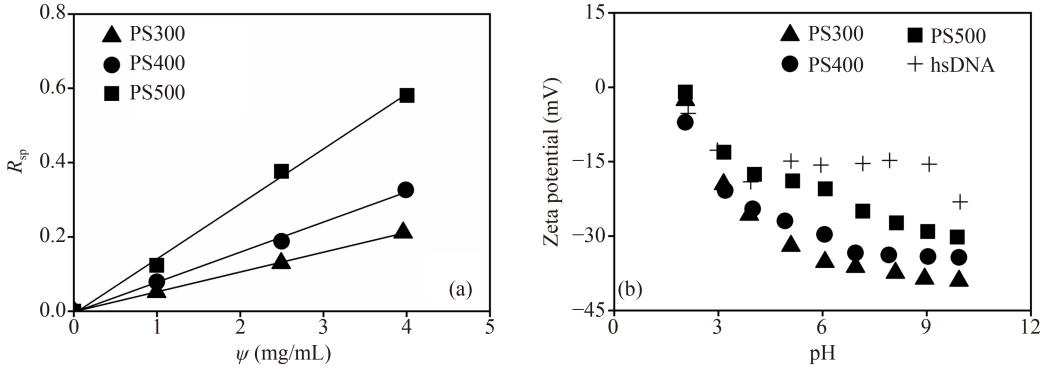

Fig. 1 R_{sp} of mixtures of water and biochar for a series of biochar concentrations (a), and zeta potential of biochars with hsDNA at a series of pH (b).

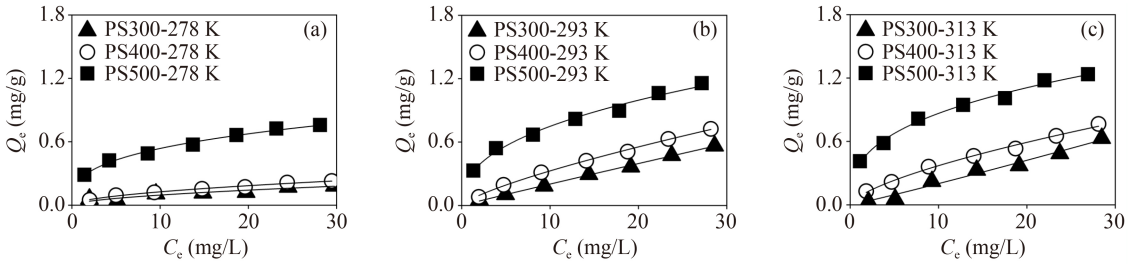

Fig. 2 Isotherms of hsDNA adsorption on PS300 (▲), PS400 (○), and PS500 (■) at 278 K (a), 293 K (b), and 313 K (c) fitted with FM.

Table 2 Fitting parameters of adsorption isotherms in LM and FM

Adsorption conditions		278 K			293 K			313 K		
		PS300	PS400	PS500	PS300	PS400	PS500	PS300	PS400	PS500
LM	Q_m	0.30	0.34	0.81	16.9	1.92	1.32	8.55	1.52	1.36
	K_l	0.05	0.06	0.25	<0.01	0.02	0.16	<0.01	0.03	0.22
	R^2	0.86	0.97	0.91	1.00	0.99	0.93	0.98	0.98	0.93
	χ^2	0.06	<0.01	0.04	<0.01	<0.01	0.08	0.04	0.03	0.10
FM	K_f	0.03	0.04	0.25	0.02	0.06	0.29	0.02	0.08	0.38
	n	0.58	0.55	0.33	0.97	0.76	0.41	1.07	0.67	0.36
	R^2	0.89	0.99	0.99	1.00	1.00	1.00	0.98	0.99	0.99
	χ^2	0.03	<0.01	<0.01	<0.01	<0.01	<0.01	0.04	<0.01	<0.01

Q_m (mg/g), K_l (L/mg), K_f ($mg^{1-1/n} \cdot L^{1/n}/g$).

in this study than traditional organic contaminants (Wang et al., 2020a) at the similar experiment condition (DNA: 2−30 mg/L; biochar: 2.5 g/L; 293 K at pH = 7). For example, 50 mL of 30 mg/L methylene blue was mixed with 0.1 g biochar under 295 K at pH = 6.5 ± 0.1 and the Q_e was about 20 mg/g (Ding et al., 2016). In addition, the Q_e was up to 6.47 mg/g for imidacloprid (20 mg/L) absorbed on biochar (2 g/L), at room temperature and pH = 7 (Zhao et al., 2018). This phenomenon probably resulted from the larger molecular sizes of DNA compared with those of such organic contaminants. The DNA used in this research was 2 nm in diameter and 17 nm in length. As shown in Fig. S2, the plentiful micropores of the biochars were smaller than 10 nm. Therefore, the micropores for small organic molecule adsorption were not available for DNA adsorption.

As shown in Fig. 2, the adsorption ability of the biochars for eDNA increased with the pyrolysis temperature. This result is probably attributable to the increase in wet surface area (Fig. 1(a)) and mesopore volume (Fig. S2) of biochar with the pyrolysis temperature. Previous studies have also shown that DNA adsorbs more on nano-biochars than on bulk-biochars because the adsorption mainly occurs on the external surface of biochar, rather than on the inner micropores, due to the large size of DNA molecules (Lian et al., 2020). Additionally, owing to the higher content of aromatic carbon, the biochar prepared at higher pyrolysis temperature preferred to interact with the pentose sugar of DNA via π–π interaction (Yuan et al., 2021), which led to higher adsorption. The negative charges on biochar surfaces significantly decreased with an increase in pyrolysis temperature (Fig. 1(b)). At the 2–11 pH range, hsDNA was also negatively charged (Fig. 1(b)). Therefore, the electrostatic repulsion between PS300 and hsDNA was much stronger than that between PS500 and hsDNA, leading to lower adsorption of hsDNA on PS300. On the other hand, phosphate is also considered a strong ligand for −OH and −COOH groups (Jelavić et al., 2018). Therefore, the phosphate backbone of DNA can directly bind with −OH groups on mineral (Hou et al., 2014) and carbon (Fang et al., 2021) surfaces via ligand exchange. The quantity of O-containing functional groups on the biochars followed the trend PS300 > PS400 > PS500 (Table 1), which was inverse of the trend for the adsorption of hsDNA on these biochars. These results implied that π–π and electrostatic interactions probably controlled the adsorption of hsDNA on biochars, rather than ligand exchange interactions.

Additionally, the adsorption nonlinearity of the isotherms increased with the pyrolysis temperature, as indicated by the decrease in n value (nonlinear index, Table 2). This result suggested an increase in the heterogeneity of biochar in the pyrolysis process. The amorphous carbon was transformed into condensed carbon in the pyrolysis process, and this was supported by the increase in aromaticity of the biochar (Table 1). Fang et al., (2021) suggested that condensed carbon increases the heterogeneity of biochar and nonlinear adsorption (Fang et al., 2021).

FTIR spectra helped understand the adsorption mechani-

sm by revealing the changes in functional groups. As shown in Fig. 3, the decrease in the height of peaks at 2920 and 2850 cm^{-1} with an increase in pyrolysis temperature suggested the loss of C–H groups (Wu et al., 2012; Wang et al., 2014b). This phenomenon was in agreement with the decrease in H/C ratio shown by elemental analysis, which implied the pyrolysis of aliphatic groups. The peaks at 1459 and 1206 cm^{-1} in the spectrum of PS300 represent the vibrations of C=O and C–O groups (Bounaas et al., 2021), which disappeared in the spectra of PS400 and PS500. The peaks at 1055 and 1035 cm^{-1} in the PS300 spectrum were derived from the deformation of C–O, indicating the presence of hydroxyl and carboxyl groups on the surface (Xiao et al., 2014). The two peaks decreased in height with an increase in the pyrolysis temperature and shifted to 1083 and 1046 cm^{-1}, respectively. Additionally, the peak at 1637 cm^{-1} was assigned to C=O stretching of biochar; this receded from PS300 to PS500 (Rajabi et al., 2021). The aforementioned phenomenon indicated the pyrolysis loss of O-containing groups in cellulose and lignin at higher temperature and was consistent with the decrease in oxygen content and polarity. The broad peak at 3442 cm^{-1} corresponded to O–H stretching (Gao et al., 2013), which resulted from the interaction between hydroxide groups and possible water remains in the biochar. The same peak was also found in the native hsDNA spectrum. In addition, the peaks at 1224 and 1062 cm^{-1} represented the vibrations of PO_2^- and PO_3^{2-} groups of hsDNA, respectively, and the peak at 1693 cm^{-1} was assigned to C=O stretching of guanine (Sheng et al., 2019). Upon hsDNA adsorption, a peak at 1384 cm^{-1} emerged in the spectra of the three biochars. Additionally, the enhancement in the intensity of this peak from PS300-DNA to PS500-DNA was in agreement with the increase in adsorption of hsDNA on the three biochars. This peak corresponded to C–H stretching on the benzene ring (Ahmad et al., 2007; Wu et al., 2019), which suggested that hsDNA adsorbed on biochar via π–π interaction with the aromatic structure.

To further clarify the role of electrostatic interaction and π–π interaction on adsorption of hsDNA on pine sawdust biochar, the adsorption of hsDNA on PS500 at a series of pH and the adsorption on PS300 and PS400 at pH = 4 were investigated. As shown in the Fig. 4(a), the adsorption capacity of hsDNA on PS5 decreased dramatically with the increase of pH from 2 to 3, and reached a steady state when pH > 4. It indicated the enhanced electrostatic repulsion between hsDNA and biochar with the pH increased, which was consistent with the increased negative potential of PS500 (Fig. 1(b)). The zeta potentials of PS300 and PS400 at pH = 4 were the

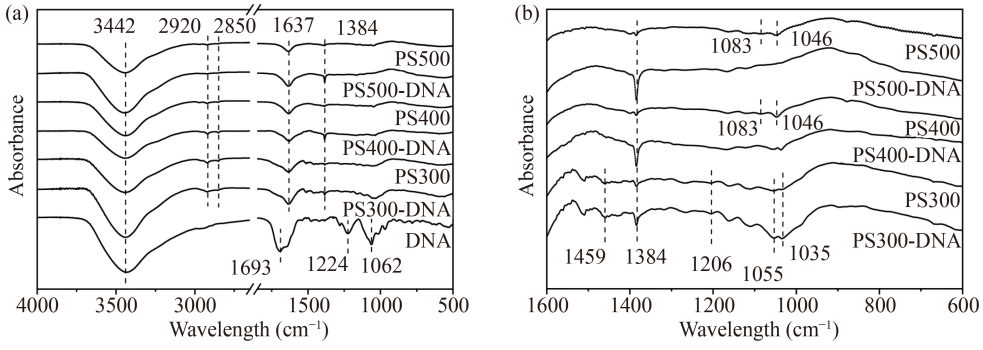

Fig. 3 (a) FTIR spectra of biochars before and after hsDNA adsorption, as well as pure hsDNA; (b) FTIR spectra of biochars in range of 1600−600 cm^{-1}.

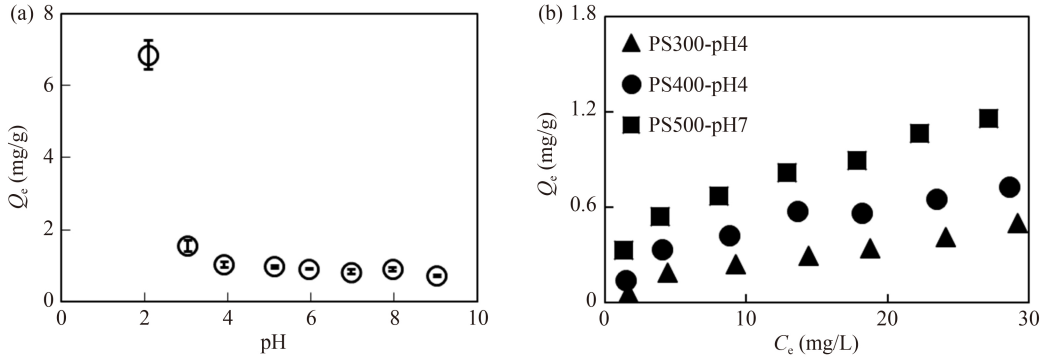

Fig. 4 The adsorption quantities of hsDNA on PS500 at pH range of 2−9 (a), and hsDNA adsorption isotherm on PS300 (▲) and PS400 (●) at pH = 4, and on PS500 (■) at pH = 7.

same with that of PS500 at pH = 7, and the zeta potential of hsDNA at pH = 4 and 7 were constant (Fig. 1(b)), indicating the comparable electrostatic repulsion between hsDNA with the three biochars. Shown by the isotherms under the circumstance (Fig. 4(b)), the adsorption capacities of PS300 and PS400 were still lower than that of PS500, verifying the stronger π–π interaction between hsDNA and the biochar prepared at higher pyrolysis temperature without the interference of electrostatic interaction.

In conclusion, the higher surface area, stronger π–π interaction, and weaker electrostatic repulsion between the biochar surface and hsDNA facilitated hsDNA adsorption on the biochars prepared at higher pyrolysis temperatures. The adsorption thermodynamics and site energy distribution are discussed in the following section to further explore the behavior of hsDNA adsorption on biochar.

3.3 Adsorption thermodynamics and site energy distribution

In-depth information regarding the inherent energy changes in the adsorption process can be supplied by thermodynamic parameters. The adsorption of hsDNA on biochar was enhanced by an increase in adsorption temperature (Fig. 2). ΔH values calculated using Eq. (7) were positive for all three biochars (Fig. 5(a)), suggesting that the adsorption was an endothermic reaction. The value of ΔH mainly varied from 8 kJ/mol to 28 kJ/mol, which was in the range of 4–167 kJ/mol, suggesting that π–π interaction was the dominant adsorption mechanism (Prasannamedha et al., 2021). In addition, ΔH values increased with the adsorption of hsDNA on PS300 and PS400, indicating that more energy was needed following an increase in hsDNA loading. However, with an increase in hsDNA adsorption on PS500, the ΔH values were basically constant and were much lower than that for the other two biochars. This suggested that the adsorption of hsDNA on PS500 was less energy-intensive, implying that the inherent adsorption site energy of PS500 was higher than that of the other two biochars. Other researchers have also noticed that a higher aromaticity of biochar facilitates the adsorption of atrazine and nicosulfuron, because of less energy demand (Wang et al., 2020b); this is discussed with the following calculated site energy distribution. As shown in Fig. 5(b), the positive ΔS values of hsDNA on the three biochars indicated that the degree of freedom of hsDNA increased.

The negative ΔG values for the three biochars indicated that the hsDNA adsorption was spontaneous and thermodynamically favorable (Fig. 5(c)) (Wang et al., 2010). The ΔG values became less negative with an increase in adsorption quantity, suggesting that the adsorption driving force became weaker. Additionally, the more negative ΔG values for hsDNA adsorption were found in range of −20 to 0 kJ/mol, with an increase in biochar pyrolysis and adsorption temperatures. These results demonstrated that the driving force of hsDNA adsorption was stronger on the surface with higher aromaticity and increased with the adsorption temperature (Chen et al., 2021).

The adsorption site energy distribution based on FM is shown in Fig. 6. The average adsorption energy E^* dramatically decreased with an increase in the quantity of hsDNA adsorbed on the three biochars (Figs. 6(a), 6(b), and 6(c)). This indicated that hsDNA firstly occupied those sites with higher energy and then had to utilize the low-energy sites owing to the heterogeneous nature of the biochar surface (Liu et al., 2012). Additionally, E^* increased with the adsorption temperature, showing that higher temperature was more beneficial to the adsorption of hsDNA on biochar. Furthermore, the E^* values of the biochars followed the trend PS500 > PS400 > PS300, which was consistent with the quantities of hsDNA adsorbed on the three biochars. According to the site energy distribution (Figs. 6(d), 6(e), and 6(f)), the trend of $F(E^*)$ of the biochars was 278 K < 293 K < 313 K, which indicated that the number of available adsorption sites of biochars at different temperatures followed the same trend. This result well explained the adsorption thermodynamics characteristics of hsDNA at different temperatures and implied that the increase in temperature probably activated some adsorption sites (Liu et al., 2019), characteristic of an endothermic reaction.

4 Conclusions

The adsorption of hsDNA on biochar was studied based

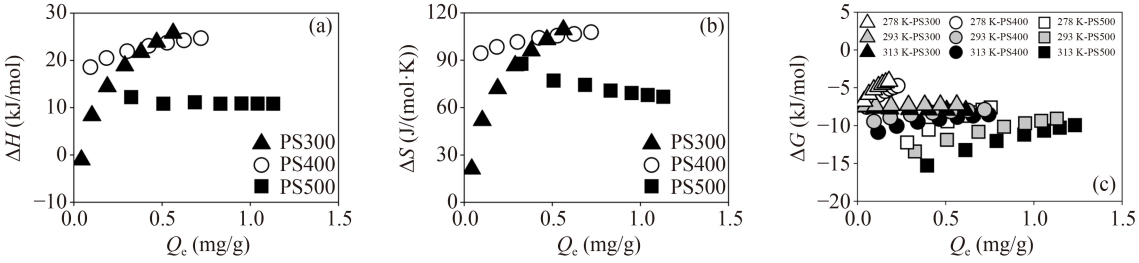

Fig. 5 Variations in ΔH (a), ΔS (b), and ΔG (c) with hsDNA adsorption on PS300 (▲), PS400 (○), and PS500 (■). ΔG values at 278, 293, and 313 K are indicated by white, grey, and black marks, respectively.

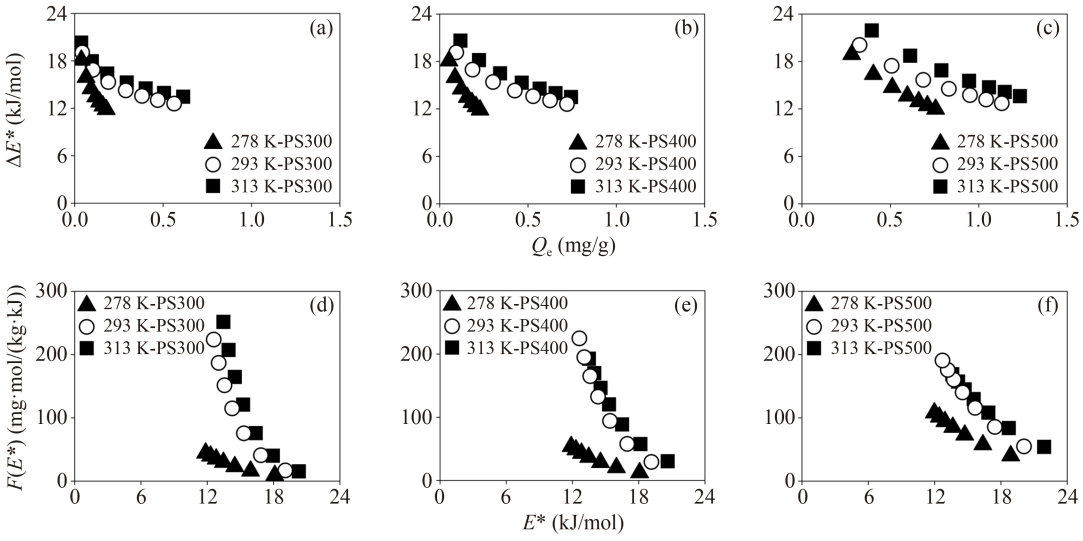

Fig. 6 Adsorption site energy of hsDNA on PS300 (a), PS400 (b), and PS500 (c) based on Q_e, and site energy distribution of hsDNA adsorption on PS300 (d), PS400 (e), and PS500 (f). All experiments were conducted under 278 K (▲), 293 K (○), 313 K (■), respectively.

on thermodynamics and site energy distribution. Compared with the properties of biochar prepared at low pyrolysis temperature, the higher surface area, stronger π–π interaction, and weaker electrostatic repulsion between hsDNA and the biochars prepared at high pyrolysis temperatures facilitated hsDNA adsorption. The thermodynamics indicated that the adsorption of hsDNA on biochar was spontaneous and endothermic. Therefore, higher temperature was beneficial for the adsorption of hsDNA on biochar, which was well explained by the increase in E^* and $F(E^*)$ with the adsorption temperature. This study improved the understanding on the effects of biochar on the environmental behavior of eDNA, and provided theoretical basis and research foundation for the subsequent research on DNA adsorption.

Acknowledgements This work was supported by the National Natural Science Foundation of China (No. 42167030), Yunnan Young and Middle-aged Academic and Technical Leaders Reserve Talents (No. 2018HB008), Yunnan Ten Thousand Talents Plan Young and Elite Talents Project (No. YNWR-QNBJ-2018-336), and Yunnan Provincial Scientific Innovation Team of Soil Environment and Ecological Safety (No. 2019HC008).

Electronic Supplementary Material Supplementary material is available in the online version of this article at https://doi.org/10.1007/s11783-022-1579-7 and is accessible for authorized users.

References

Ahmad A, Loh M, Aziz J (2007). Preparation and characterization of activated carbon from oil palm wood and its evaluation on methylene blue adsorption. Dyes and Pigments, 75(2): 263–272

Bounaas M, Bouguettoucha A, Chebli D, Gatica J M, Vidal H (2021). Role of the wild carob as biosorbent and as precursor of a new high-surface-area activated carbon for the adsorption of methylene blue. Arabian Journal for Science and Engineering, 46(1): 325–341

Cai P, Huang Q, Li M, Liang W (2008). Binding and degradation of DNA on montmorillonite coated by hydroxyl aluminum species. Colloids and Surfaces. B, Biointerfaces, 62(2): 299–306

Chen B, Zhou D, Zhu L (2008). Transitional adsorption and partition of nonpolar and polar aromatic contaminants by biochars of pine needles with different pyrolytic temperatures. Environmental Science & Technology, 42(14): 5137–5143

Chen H, Zhang Y, Li J, Zhang P, Liu N (2019). Preparation of pickling-reheating activated alfalfa biochar with high adsorption efficiency for p-nitrophenol: characterization, adsorption behavior, and mechanism. Environmental Science and Pollution Research International, 26(15): 15300–15313

Chen Y, Liu J, Zeng Q, Liang Z, Ye X, Lv Y, Liu M (2021). Preparation of *Eucommia ulmoides* lignin-based high-performance biochar containing sulfonic group: Synergistic pyrolysis mechanism and tetracycline hydrochloride adsorption. Bioresource Technology, 329: 124856

Ding Z, Wan Y, Hu X, Wang S, Zimmerman A R, Gao B (2016). Sorption of lead and methylene blue onto hickory biochars from different pyrolysis temperatures: Importance of physicochemical properties. Journal of Industrial and Engineering Chemistry, 37: 261–267

Dong X, Singh B P, Li G, Lin Q, Zhao X (2019). Biochar increased field soil inorganic carbon content five years after application. Soil & Tillage Research, 186: 36–41

Fang J, Jin L, Meng Q, Wang D, Lin D (2021). Interactions of extracellular DNA with aromatized biochar and protection against degradation by DNAse I. Journal of Environmental Sciences (China), 101: 205–216

Gao N, Li A, Quan C, Du L, Duan Y (2013). TG–FTIR and Py–GC/MS analysis on pyrolysis and combustion of pine sawdust. Journal of Analytical and Applied Pyrolysis, 100: 26–32

Gardner C M, Gunsch C K (2017). Adsorption capacity of multiple DNA sources to clay minerals and environmental soil matrices less

than previously estimated. Chemosphere, 175: 45–51

Hong M, Zhang L, Tan Z, Huang Q (2019). Effect mechanism of biochar's zeta potential on farmland soil's cadmium immobilization. Environmental Science and Pollution Research International, 26(19): 19738–19748

Hou Y, Wu P, Zhu N (2014). The protective effect of clay minerals against damage to adsorbed DNA induced by cadmium and mercury. Chemosphere, 95: 206–212

Jelavić S, Stipp S L S, Bovet N (2018). Adsorption of organic ligands on low surface charge clay minerals: the composition in the aqueous interface region. Physical Chemistry Chemical Physics, 20(25): 17226–17233

Jiang S, Nguyen T A, Rudolph V, Yang H, Zhang D, Ok Y S, Huang L (2017). Characterization of hard- and softwood biochars pyrolyzed at high temperature. Environmental Geochemistry and Health, 39(2): 403–415

Leng L, Xiong Q, Yang L, Li H, Zhou Y, Zhang W, Jiang S, Li H, Huang H (2021). An overview on engineering the surface area and porosity of biochar. Science of the Total Environment, 763: 144204

Levy-Booth D J, Campbell R G, Gulden R H, Hart M M, Powell J R, Klironomos J N, Peter Pauls K, Swanton C J, Trevors J T, Dunfield K E (2007). Cycling of extracellular DNA in the soil environment. Soil Biology & Biochemistry, 39(12): 2977–2991

Lian F, Yu W, Zhou Q, Gu S, Wang Z, Xing B (2020). Size matters: Nano-biochar triggers decomposition and transformation inhibition of antibiotic resistance genes in aqueous environments. Environmental Science & Technology, 54(14): 8821–8829

Liu F, Wang S, Fan J, Ma G (2012). Adsorption of natural organic matter surrogates from aqueous solution by multiwalled carbon nanotubes. Journal of Physical Chemistry C, 116(49): 25783–25789

Liu J, Zhou B, Zhang H, Ma J, Mu B, Zhang W (2019). A novel Biochar modified by Chitosan-Fe/S for tetracycline adsorption and studies on site energy distribution. Bioresource Technology, 294: 122152

Liu T, Wang Y, Zang Q, Zhong G (2018a). Hydrothermal synthesis, structural characterization, and interaction mechanism with DNA of Copper(II) complex containing 2,2′-bipyridine. Bioinorganic Chemistry and Applications, 2018: 8459638

Liu Y, Dai Q, Jin X, Dong X, Peng J, Wu M, Liang N, Pan B, Xing B (2018b). Negative impacts of biochars on urease activity: High pH, heavy metals, polycyclic aromatic hydrocarbons, or free radicals? Environmental Science & Technology, 52(21): 12740−12747

Min X, Han P, Yang H, Kim H, Tong M (2014). Influence of sulfate and phosphate on the deposition of plasmid DNA on silica and alumina-coated surfaces. Colloids and Surfaces. B, Biointerfaces, 118: 83−89

Pan B, Zhang D, Li H, Wu M, Wang Z, Xing B (2013). Increased adsorption of sulfamethoxazole on suspended carbon nanotubes by dissolved humic acid. Environmental Science & Technology, 47(14): 7722–7728

Pietramellara G, Ascher J, Ceccherini M T, Nannipieri P, Wenderoth D (2007). Adsorption of pure and dirty bacterial DNA on clay minerals and their transformation frequency. Biology and Fertility of Soils, 43(6): 731–739

Poly F, Chenu C, Simonet P, Rouiller J, Jocteur Monrozier L (2000). Differences between linear chromosomal and supercoiled plasmid DNA in their mechanisms and extent of adsorption on clay minerals. Langmuir, 16(3): 1233–1238

Prasannamedha G, Kumar P S, Mehala R, Sharumitha T J, Surendhar D (2021). Enhanced adsorptive removal of sulfamethoxazole from water using biochar derived from hydrothermal carbonization of sugarcane bagasse. Journal of Hazardous Materials, 407: 124825

Pruden A, Pei R, Storteboom H, Carlson K H (2006). Antibiotic resistance genes as emerging contaminants: studies in northern Colorado. Environmental Science & Technology, 40(23): 7445–7450

Qian L, Zhang W, Yan J, Han L, Gao W, Liu R, Chen M (2016). Effective removal of heavy metal by biochar colloids under different pyrolysis temperatures. Bioresource Technology, 206: 217–224

Rajabi H, Mosleh M H, Mandal P, Lea-Langton A, Sedighi M (2021). Sorption behaviour of xylene isomers on biochar from a range of feedstock. Chemosphere, 268: 129310

Schmidt M P, Martínez C E (2017). Ironing out genes in the environment: An experimental study of the DNA-goethite interface. Langmuir, 33(34): 8525–8532

Sheng X, Qin C, Yang B, Hu X, Liu C, Waigi M G, Li X, Ling W (2019). Metal cation saturation on montmorillonites facilitates the adsorption of DNA via cation bridging. Chemosphere, 235: 670–678

Shi L, Zhang D, Zhao J, Xue J, Yin M, Liang A, Pan B (2021). New insights into the different adsorption kinetics of gallic acid and tannic acid on minerals via ^{1}H NMR relaxation of bound water. Science of the Total Environment, 767: 144447

Teixidó M, Pignatello J J, Beltrán J L, Granados M, Peccia J (2011). Speciation of the ionizable antibiotic sulfamethazine on black carbon (biochar). Environmental Science & Technology, 45(23): 10020–10027

Wang B, Zhang Y, Zhu D, Li H (2020a). Assessment of bioavailability of biochar-sorbed tetracycline to *Escherichia coli* for activation of antibiotic resistance genes. Environmental Science & Technology, 54(20): 12920–12928

Wang C, Wang T, Li W, Yan J, Li Z, Ahmad R, Herath S K, Zhu N (2014a). Adsorption of deoxyribonucleic acid (DNA) by willow wood biochars produced at different pyrolysis temperatures. Biology and Fertility of Soils, 50(1): 87–94

Wang P, Liu X, Yu B, Wu X, Xu J, Dong F, Zheng Y (2020b). Characterization of peanut-shell biochar and the mechanisms underlying its sorption for atrazine and nicosulfuron in aqueous solution. Science of the Total Environment, 702: 134767

Wang Y, Yin R, Liu R (2014b). Characterization of biochar from fast pyrolysis and its effect on chemical properties of the tea garden soil. Journal of Analytical and Applied Pyrolysis, 110: 375–381

Wang Z, Yu X, Pan B, Xing B (2010). Norfloxacin sorption and its thermodynamics on surface-modified carbon nanotubes. Environmental Science & Technology, 44(3): 978–984

Wu J, Wang H, Zhu A, Long F (2018). Adsorption kinetics of single-stranded DNA on functional silica surfaces and its influence factors: An evanescent-wave biosensor study. ACS Omega, 3(5): 5605–5614

Wu J, Wang T, Zhang Y, Pan W P (2019). The distribution of Pb(II)/Cd(II) adsorption mechanisms on biochars from aqueous

solution: Considering the increased oxygen functional groups by HCl treatment. Bioresource Technology, 291: 121859

Wu W, Yang M, Feng Q, Mcgrouther K, Wang H, Lu H, Chen Y (2012). Chemical characterization of rice straw-derived biochar for soil amendment. Biomass and Bioenergy, 47: 268–276

Xiao X, Chen B, Zhu L (2014). Transformation, morphology, and dissolution of silicon and carbon in rice straw-derived biochars under different pyrolytic temperatures. Environmental Science & Technology, 48(6): 3411–3419

Yin D, Wang X, Chen C, Peng B, Tan C, Li H (2016). Varying effect of biochar on Cd, Pb and As mobility in a multi-metal contaminated paddy soil. Chemosphere, 152: 196–206

Yu W, Li N, Tong D, Zhou C, Lin C, Xu C (2013). Adsorption of proteins and nucleic acids on clay minerals and their interactions: A review. Applied Clay Science, 80−81: 443–452

Yuan L, Chen L, Chen X, Liu R, Ge G (2017). In situ measurement of surface functional groups on silica nanoparticles using solvent relaxation nuclear magnetic resonance. Langmuir, 33(35): 8724–8729

Yuan Y, Li J, Dai H (2021). Microcystin-LR sorption and desorption by diverse biochars: Capabilities, and elucidating mechanisms from novel insights of sorption domains and site energy distribution. Science of the Total Environment, 754: 141921

Zhang L, Li H, Chen F, Zhang D, Wu M, Pan B, Xing B (2017). New insights provided by solvent relaxation NMR-measured surface area in liquids to explain phenolics sorption on silica nanoparticles. Environmental Science. Nano, 4(3): 577–584

Zhang Q, Peng Q, Shu X, Mo D, Jiang D (2019). Spectroscopic analysis of tylosin adsorption on extracellular DNA reveals its interaction mechanism. Colloids and Surfaces. B, Biointerfaces, 183: 110431

Zhao R, Ma X, Xu J, Zhang Q (2018). Removal of the pesticide imidacloprid from aqueous solution by biochar derived from peanut shell. BioResources, 13(3): 5656–5669

Zhong W, Yu J, Liang Y (2003). Chlorobenzylidine-herring sperm DNA interaction: Binding mode and thermodynamic studies. Spectrochimica Acta. Part A: Molecular and Biomolecular Spectroscopy, 59(6): 1281–1288

Zhou G, Qiu X, Wu X, Lu S (2021). Horizontal gene transfer is a key determinant of antibiotic resistance genes profiles during chicken manure composting with the addition of biochar and zeolite. Journal of Hazardous Materials, 408: 124883